

# Journal of Geophysical Research: Oceans

## RESEARCH ARTICLE

10.1002/2015JC011131

### Special Section:

Pacific-Asian Marginal Seas

#### Key Points:

- Long-term observations show ITs are the strongest in winter near Luzon Strait
- Kuroshio intrusion and nonlinear interaction of ITs enhance ITs
- Energy of semidiurnal ITs in upper layer is carried downward to lower layer

#### Correspondence to:

S. Cai,  
caisq@scsio.ac.cn

#### Citation:

Liu, J., Y. He, D. Wang, T. Liu, and S. Cai (2015), Observed enhanced internal tides in winter near the Luzon Strait, *J. Geophys. Res. Oceans*, 120, 6637–6652, doi:10.1002/2015JC011131.

Received 10 JUL 2015

Accepted 15 SEP 2015

Accepted article online 21 SEP 2015

Published online 12 OCT 2015

## Observed enhanced internal tides in winter near the Luzon Strait

**Junliang Liu<sup>1</sup>, Yinghui He<sup>1</sup>, Dongxiao Wang<sup>1</sup>, Tongya Liu<sup>1,2</sup>, and Shuqun Cai<sup>1</sup>**

<sup>1</sup>State Key Laboratory of Tropical Oceanography, South China Sea Institute of Oceanology, Chinese Academy of Sciences, Guangzhou, China, <sup>2</sup>Graduate School, Chinese Academy of Sciences, Beijing, China

**Abstract** Seasonal characteristics and nonlinear interaction of internal tides (ITs) near the Luzon Strait in the northeastern South China Sea are investigated using 285 day, in situ observation data. It is found that ITs, which are dominated by the first-mode wave throughout the year, are the strongest in subsurface layer. Baroclinic incoherent diurnal (semidiurnal) variance accounts for about 85.7% (78.3%) of diurnal (semidiurnal) ITs. The amplitude and seasonal variation of the diurnal ITs are more prominent than those that are semidiurnal, e.g., the largest kinetic energy densities of diurnal and semidiurnal baroclinic tidal currents are 2.81 and 0.83 KJ/m<sup>2</sup> in winter, respectively. It is considered that there are two reasons for the significantly enhanced ITs in winter: (1) it may be due to the Kuroshio intrusion, and (2) the enhanced diurnal ITs may be due to the enhanced diurnal barotropic tidal currents, while the enhanced semidiurnal ITs may be caused by the strong nonlinear interaction between diurnal IT constituents  $O_1$  and  $K_1$  due to their high vertical shears in subsurface layer. Thus, harmonic semidiurnal constituent  $D_2$  with a similar frequency of constituent  $M_2$  is induced; it subsequently enhances the semidiurnal ITs in this subsurface layer, and the associated energy is carried downward to enhance the semidiurnal ITs in the upper and lower layers.

## 1. Introduction

Internal tides (ITs) are a significant physical oceanographic phenomenon. Notably, ITs play a crucial role in large-scale oceanographic contexts, as it is widely recognized that they are associated closely with diapycnal mixing processes in the deep ocean [Garrett and Munk, 1972, 1975]. Higher-mode ITs usually break and dissipate near their source regions and thus generate local ocean mixing [Vlasenko et al., 2010; Klymak et al., 2011], whereas low-mode ITs may propagate for thousands of kilometers before dissipating and usually dominate further from the source region [St. Laurent and Garrett, 2002]. To date, most studies indicate that the first-mode waves dominate the IT field, although higher-mode signals may be significant in specific cases or over short periods, i.e., sometimes higher-mode signals may be more prominent than or comparable to those with lower modes [Xu et al., 2013]. Moreover, after long propagation from the source region, low-mode ITs interact with background conditions and integrate the effect through variable stratification and mesoscale activity [Park et al., 2006]. Then, they may exhibit intermittent feature and occur at frequencies outside the deterministic tidal frequencies, becoming incoherent (i.e., not phase-locked to the astronomical forcing) with the astronomical tides. Recent studies [Lee et al., 2012; Xu et al., 2013] present the incoherent structure of diurnal and semidiurnal ITs in the northern South China Sea (SCS) based on moored velocity observation for several months. The results from these studies showed that the phase and amplitude of diurnal and semidiurnal ITs varied irregularly in fortnightly cycle which related to spring and neap tides. The reason causing irregular structure may be related to the varied stratification due to eddies, Kuroshio intrusion, and etc. Those studies indicated that the incoherent structure plays an important role on ITs which may account for over 50% variance of IT energy.

Located in the northeast of the SCS, the Luzon Strait (LS) is the primary passage connecting the SCS to the northwest Pacific Ocean and has complex topography. When the westward barotropic tides pass through the LS, the interaction of barotropic tidal currents with the abruptly changing topography will thus generate strong ITs. However, former studies on ITs of the SCS based on long-term, in situ observations are mainly restricted to east of the Dongsha Islands [Cai et al., 2002; Lee et al., 2012; Xu et al., 2013], whereas those near the LS are relatively rare. Lien et al. [2005] confirm that the strong ITs are generated

near the LS, then propagate as a narrow tidal beam into the SCS which are amplified by the shoaling continental slope near the Dongsha Islands, and finally evolve into high-frequency, nonlinear internal waves. *Liao et al.* [2011] find that the ITs in the upper layer of the LS are a mixed type, the semidiurnal ITs are mainly first mode, and the diurnal ITs are nearly second mode. However, the seasonal characteristics of ITs near the LS have been rarely addressed due to limited in situ observations over the long term. Based on two 9 month mooring ADCP data sets west of the LS, *Xu et al.* [2014] find that the diurnal ITs are stronger in summer and winter but weaker in spring and autumn, and both diurnal and semidiurnal ITs contain stronger coherent signals than incoherent counterparts at two sites. However, as concluded by *Cai et al.* [2015], since the sampling resolution of their observed current data sets (1h) is too low, thus some incoherent information due to the nonlinear interaction of internal solitary waves and Kuroshio intrusion, etc. cannot be revealed by data sets.

Nonlinear interactions provide a link to transfer large-scale, internal wave energy to small dissipation scales which can directly induce ocean mixing [*Muller et al.*, 1986]. There are primarily two types of interactions that have been identified in the ocean, resonant (weakly wave-wave) and nonresonant (strong) interactions. Currently, nonresonant interactions are found to mainly occur between near-inertial waves and ITs [*Xing and Davies*, 2002; *van Haren*, 2004]. *Alford* [2008] suggests that the occurrence of parametric subharmonic instability (PSI) of diurnal ITs at "critical" latitudes of 14.52°N and 13.44°N in the SCS, respectively. *Xie et al.* [2010] study nonlinear interactions among internal tidal waves in the northeastern SCS near the LS and find that the freely propagating M<sub>2</sub> internal tidal wave plays the most crucial role in these interactions. *Sun et al.* [2011] find that the typhoon-induced near-inertial waves could resonate with diurnal ITs in the western SCS, where the local inertial frequency is nearly half of the diurnal one.

To date, few studies on ITs based on long-term observations near the west side of LS in the northeastern SCS have been reported. Thus, this study uses 285 day, long-term in situ acoustic Doppler current profiler (ADCP) observations with a high sampling resolution of 2 min near the LS to investigate several issues, i.e., What is the seasonal variation of ITs near the LS? How does the modal structure of ITs vary with season? Is there any nonlinear interaction of ITs near the LS? In this paper, data and computational methods are presented in section 2. Section 3 discussed the results and discussion, followed by the conclusions in section 4.

## 2. Data and Methods

### 2.1. Data

An up-looking broadband 76.8 Khz RDI ADCP is moored at a depth of about 501 m under the water at (19°28'N, 119°57'E) near the LS in the northeastern SCS (Figure 1). At this location, the water depth is about 4054 m. The ADCP measures the current velocity from 29 to 501 m, with a depth interval of 8 m and a ping rate of 120 s. The effective data range is from 53 to 501 m. Pressure data recorded using the ADCP show that the instrument depth fluctuated several tens of meters and occasionally as much as 100 m. The instrument was mounted at an averaged depth of 520 m. The time series of current are treated as stable ADCP depth after these offsets were corrected. In this study, the duration of observation is from 20 September 2008 to 3 July 2009. The current data are averaged hourly for further analysis.

### 2.2. Methods

The barotropic current is defined as the depth-averaged flow which is different from that predicted by TPXO7.1 (TOPEX/POSEIDON global tidal model) [*Egbert and Erofeeva*, 2002; *Xu et al.*, 2014], and the baroclinic current as the residual once the barotropic current is removed. The diurnal (semidiurnal) tidal currents are obtained by band-pass filters from the observed current data. The upper and lower cutoff frequencies of band-pass filters for diurnal (semidiurnal) tidal currents are 0.8 and 1.2 times the diurnal (semidiurnal) frequency, respectively. Harmonic analysis is performed using the MATLAB T\_Tide program [*Pawlowicz et al.*, 2002] to obtain harmonic constants at each bin depth, which also is applied to the entire baroclinic record period to extract the diurnal (semidiurnal) ITs that is coherent; we subtract the coherent components from the raw baroclinic diurnal (semidiurnal) current to obtain the incoherent diurnal (semidiurnal) current [*Lee et al.*, 2012; *Xu et al.*, 2013]. The empirical orthogonal function (EOF) method is employed to characterize the detailed seasonal vertical modal structure of ITs [*Lee et al.*, 2012; *Xu et al.*, 2013].

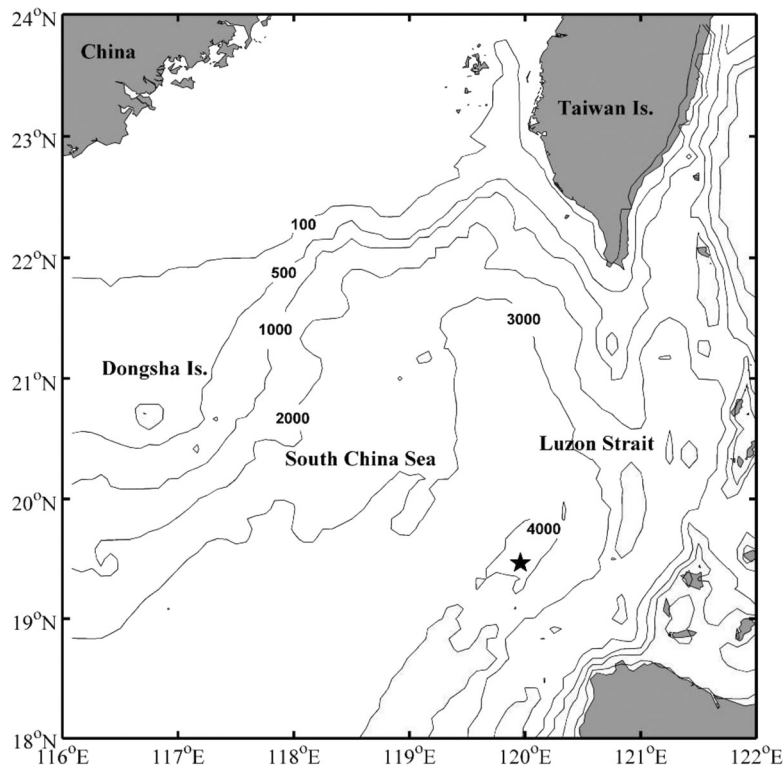


**Figure 1.** Map of the observation site near the LS in the SCS (where the star denotes the observation site, and the unit of the bottom topography contour is m).

The power spectra densities (PSDs) of the four major tidal constituents ( $O_1$ ,  $K_1$ ,  $M_2$ , and  $S_2$ ) are defined as

$$PSD = \sqrt{PSD_u^2 + PSD_v^2}, \quad (1)$$

where  $PSD_u$  and  $PSD_v$  are the PSDs of the  $u$  and  $v$  components of the four major tidal constituents, respectively.

The depth-integrated kinetic energy density (KED) is computed as

$$KED = \frac{1}{2} \rho \int_{H_1}^{H_2} U^2(z) dz, \quad (2)$$

where  $\rho$  is the vertical average seawater density,  $U$  is the current speed,  $H_1$  and  $H_2$  are the lower and upper limits of the computed depths (here  $H_1 = 53$  m and  $H_2 = 501$  m), respectively. KEDs of band-pass filtered, diurnal (semidiurnal) baroclinic tidal currents are also calculated. Moreover, continuous wavelet transform is used to obtain the power spectra of currents and reveal the distribution of internal tidal kinetic energy (KE) in time and frequency domains.

Bicoherence spectrum (normalized bispectrum) is important in the nonlinear interaction analysis [van Haren, 2005; Carter and Gregg, 2006; Xie et al., 2008]. It is used to distinguish the extent of quadratic phase coupling in a deterministic signal from independently excited waves. To ascertain the extent of nonlinear coupling among internal tidal currents, the higher-order spectral analysis method, bicoherence method, is also used [Kim and Powers, 1979]. The bispectrum is the frequency domain representation of the third-order cumulant, and the bicoherence is normalized representation of the bispectrum defined as

$$b^2(\omega_1, \omega_2) = |B(\omega_1, \omega_2)|^2 / p(\omega_1) \cdot p(\omega_2) \cdot p(\omega_1 + \omega_2), \quad (3)$$

where  $B(\omega_1, \omega_2)$  is the bispectrum and  $p(\omega)$  is the power spectrum. This statistic is used for the study of nonlinear interactions [Elgar and Guza, 1988; van Haren, 2005]. A large bicoherence value generally suggests a stronger nonlinear coupling between two frequencies,  $\omega_1$  and  $\omega_2$  [Hinich and Wolinsky, 2005].

The wave number rotary spectrum is employed to reveal the energy propagation direction of ITs. Based on the definition and method proposed by *Leaman and Sanford* [1975], the vertical distribution of the horizontal velocity vectors can be written as the form of  $u(z) + iv(z)$  corresponding to the vertical wave number  $m$ ,

$$u(z) + iv(z) = \frac{1}{d} \int_0^d (u + iv) e^{-imz} dz, \quad (4)$$

where  $d$  is the water depth. It can be divided into two parts with the positive and the negative wave numbers,

$$u_m + iv_m = u_+ e^{+imz} + u_- e^{-imz}, \quad (5)$$

where  $u_-$  and  $u_+$  are the clockwise and anticlockwise rotary components, respectively. The spectra of the clockwise and anticlockwise rotary components are,

$$\begin{cases} C_m = \frac{1}{2} \langle u_-^* u_- \rangle \\ A_m = \frac{1}{2} \langle u_+^* u_+ \rangle \end{cases}, \quad (6)$$

where  $C_m$  ( $A_m$ ) is the clockwise (anticlockwise) rotary spectrum, angular brackets denote the parameters within are averaged, and stars denote the complex conjugate.  $C_m$  ( $A_m$ ) indicates how intensively the wave energy is propagating downward (upward), and the energy propagation is indicated by  $C_m$ - $A_m$ . If  $C_m$ - $A_m$  is positive (negative), then it indicates that the energy propagates downward (upward) and the energy source locates at the ocean surface (bottom).

The shear magnitude of current velocity is defined as,

$$S = \sqrt{\left(\frac{\partial u}{\partial z}\right)^2 + \left(\frac{\partial v}{\partial z}\right)^2}, \quad (7)$$

where  $u$  and  $v$  are the eastward and northward components of the current velocity, respectively.

In order to study the seasonal characteristics of ITs near the LS, the whole observation period is divided into four stages: stage 1 (autumn) is from 20 September 2008 to 30 November 2008; stage 2 (winter) is from 1 December 2008 to 28 February 2009; stage 3 (spring) is from 1 March 2009 to 31 May 2009; and stage 4 (summer) is from 1 June 2009 to 3 July 2009. For convenience, three depth ranges (53–205 m), (213–365 m), and (373–501 m) are chosen to represent subsurface, upper and lower layers of the observed ocean, respectively.

### 3. Results and Discussion

#### 3.1. Basic Characteristics

The wavelet power spectra of observed total currents are estimated to illustrate the temporal and frequency distributions of the KE field at our observation site (Figure 2). Diurnal tidal currents can be easily found in these three layers with high-power signals around a period of 1 day, whereas semidiurnal ones are only relatively strong in the subsurface layer. Moreover, 14 day, spring neap oscillations can also be seen throughout the year, with currents being strong and then weak periodically. These fortnightly oscillations indicate significant diurnal ITs at our observational site. Moreover, rotary spectra of the raw currents in the whole water columns during the entire record are calculated (figure not shown). It is found that the current spectra show significant peaks at the near-inertial, diurnal, and semidiurnal frequencies, with dominant clockwise rotation.

The barotropic tidal currents are dominated by two main diurnal constituents,  $K_1$  and  $O_1$ , followed by two semidiurnal constituents  $M_2$  and  $S_2$  (Table 1 and Figures 3a–3d). The diurnal constituents are much more remarkable than the semidiurnal ones. The semimajor axis of barotropic  $O_1$  reaches a maximum of 10.1 cm/s, which is close to that of  $K_1$  (10 cm/s). The results are similar to those reported by *Liao et al.* [2011], but somewhat larger than those by *Xu et al.* [2013]. The  $M_2$  tidal current ellipse has an amplitude of roughly half that of  $K_1$ ; the  $S_2$  tidal current ellipse has the weakest amplitude, roughly half that of  $M_2$ , which is different

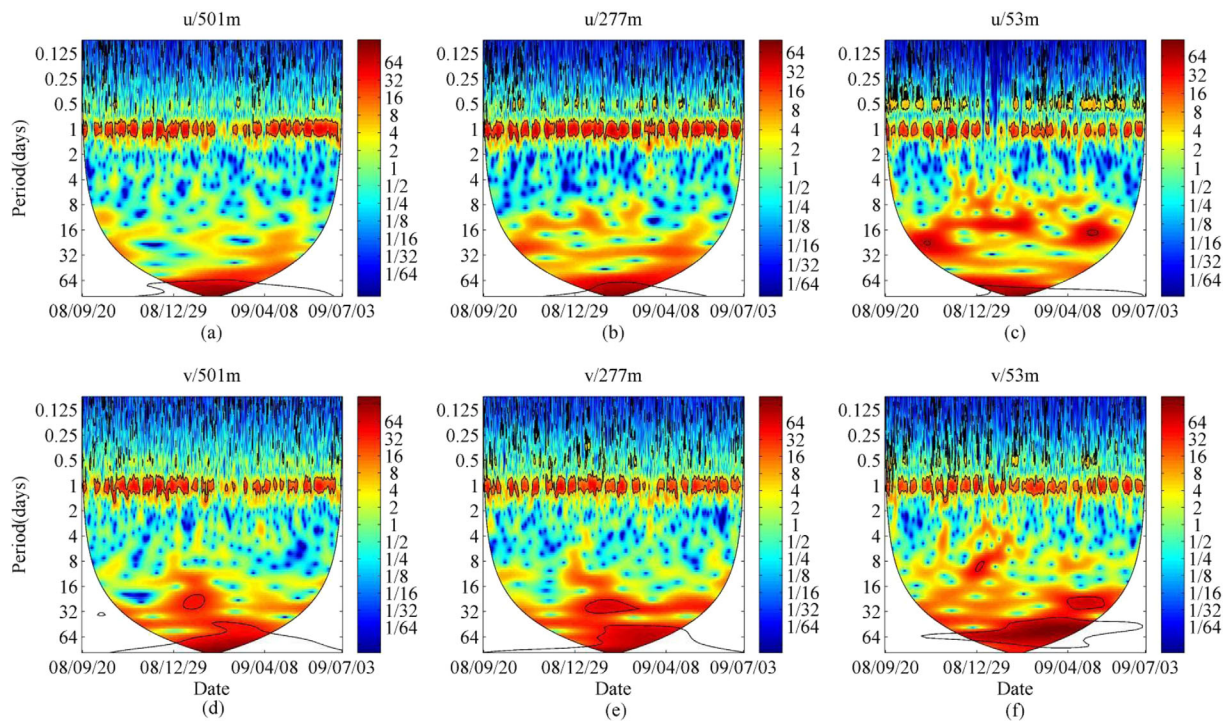


**Figure 2.** Continuous wavelet power spectra of (a–c)  $u$  and (d–f)  $v$  components of total observed currents at depths of (a, d) 501 m, (b, e) 277 m, and (c, f) 53 m, respectively. The thick black lines denote the 95% confidence level, and the thin black lines indicate the region affected by the edges of data. The units on the color bar scale are nominal. The time axis is in the format of year/month/day.

from those reported by *Lee et al.* [2012]. Negative semiminor axes indicate that the barotropic constituents  $K_1$ ,  $O_1$ , and  $S_2$  all rotate clockwise, whereas positive semiminor axis shows that the barotropic constituent  $M_2$  rotates counterclockwise. Furthermore, based on the amplitudes of harmonic constants of constituents  $K_1$ ,  $O_1$ , and  $M_2$ , the ratio  $(H_{K1} + H_{O1})/H_{M2}$ , which is equal to 3.4, shows that the barotropic tidal currents are mixed, diurnal dominant (here  $H$  represents the tidal harmonic constant). For ITs, the diurnal constituents are also prominent (Figures 3e and 3f). The semimajor axes of baroclinic constituents  $O_1$ ,  $K_1$ ,  $M_2$ , and  $S_2$  all reach their maximum around a depth of 61 m, with values of 14.0, 10.1, 7.7, and 3.3 cm/s, respectively. Moreover, based on the ratio  $(H_{K1} + H_{O1})/H_{M2}$ , it is found that the tidal nature of ITs changes with depth, e.g., ITs are mixed, diurnal dominant from 53 to 229 m, diurnal type from 237 to 301 m and mixed, semidiurnal dominant below 309 m.

We also calculate the time averages of variances of coherent and incoherent components of the diurnal and semidiurnal ITs (Figure 4). The  $u$  ( $v$ ) component of baroclinic incoherent diurnal variance accounts for about 85.7% (84.8%) of diurnal ITs, while the semidiurnal tidal variance contains a similar fraction 78.3% (91.9%) of the semidiurnal ITs. Our results are in conflict with those of *Xu et al.* [2014]. The guess that different barotropic tidal currents used by both studies result in different conclusions is excluded after we replace the observed barotropic velocity with TPXO which is the same barotropic tidal currents used by *Xu et al.* [2014]. Therefore, the different sampling resolutions may be the most possible reason for causing the conflict results on the coherent and incoherent structures of ITs between the two studies. Furthermore, it is found that barotropic currents calculated by using the observed velocity in the upper 501 m at our observational site exhibit a larger amplitude and a more striking seasonal variation than those by using TPXO

**Table 1.** Tidal Ellipse Parameters of the Four Primary Barotropic Constituents

Constituents	Semimajor Axis (cm/s)	Seminor Axis (cm/s)	Inclination (°)	Lag (°)
$K_1$	10.0	-4.8	14.92	110.68
$O_1$	10.1	-4.5	30.71	50.18
$M_2$	5.9	0.7	161.78	195.86
$S_2$	3.0	-0.4	162.75	231.01

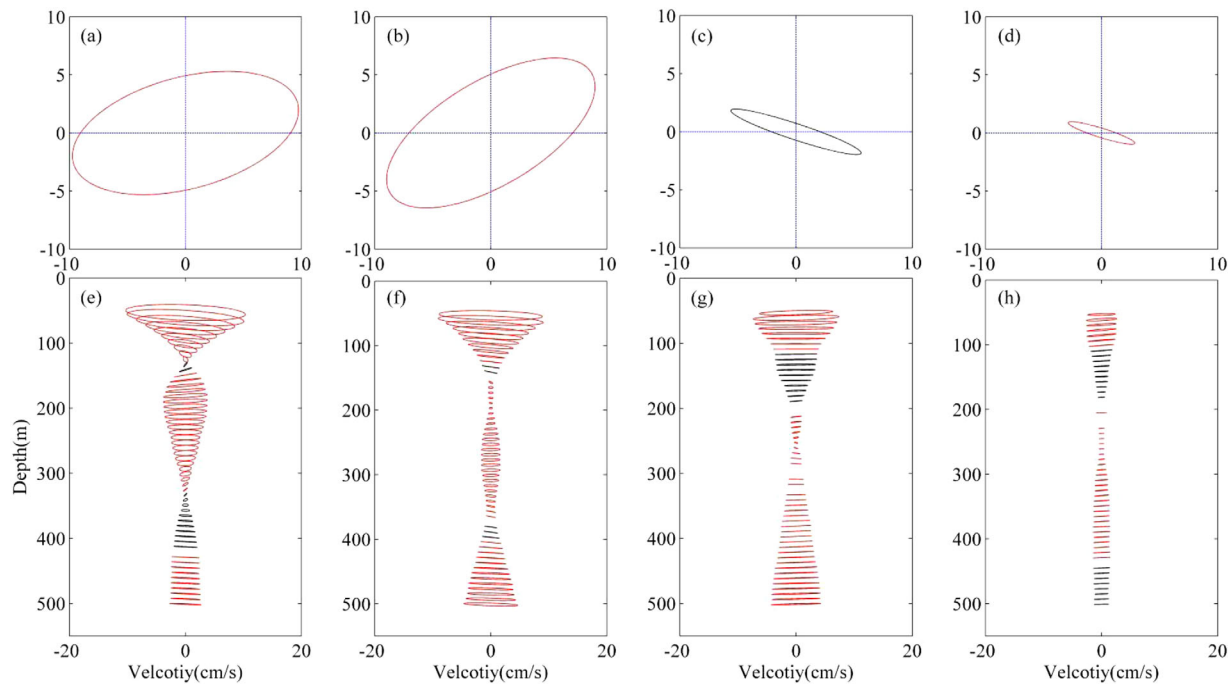


**Figure 3.** (a–d) Barotropic and (e–f) baroclinic tidal current ellipses of the four primary constituents (a, e)  $K_1$ , (b, f)  $O_1$ , (c, g)  $M_2$ , and (d, h)  $S_2$ . The clockwise and counter-clockwise tidal ellipses are marked in red and black, respectively.

during the whole observational period (Figure 5), i.e., TPXO data may somewhat underestimate the barotropic currents in the LS. Moreover, it is found that the diurnal and semidiurnal coherent and incoherent motions all display a first-mode structure in the vertical.

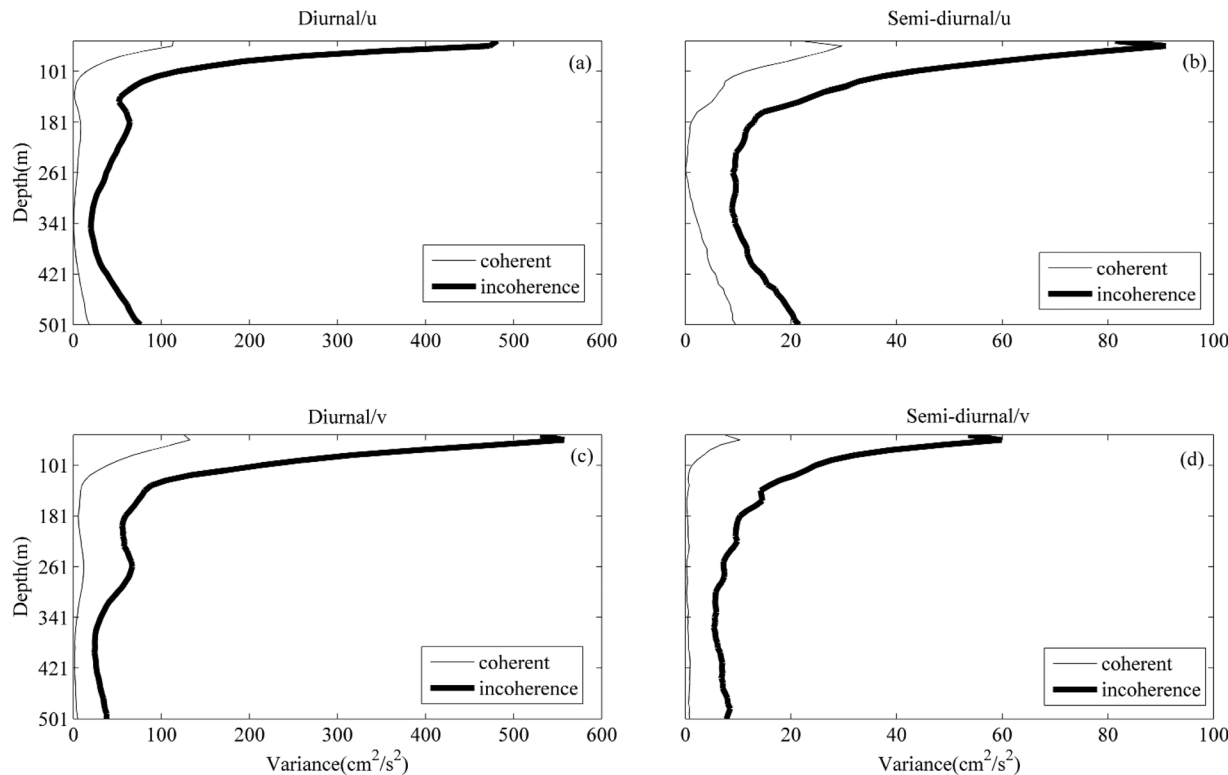


**Figure 4.** Temporal mean coherent and incoherent current variances of (a, b)  $u$  and (c, d)  $v$  components of (a, c) diurnal and (b, d) semidiurnal ITs during entire record period, respectively.

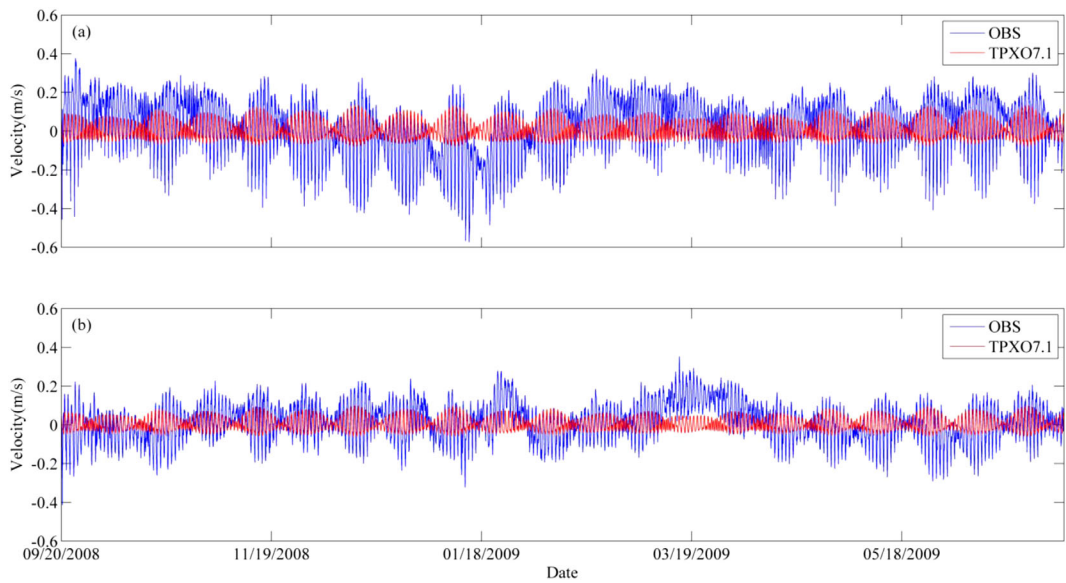


**Figure 5.** Comparison of the (a)  $u$  and (b)  $v$  components of the barotropic current calculated by TPXO7.1 and depth-averaged current, respectively. The time axis is in the format of month/day/year.

### 3.2. Seasonal, Monthly Characteristics of ITs and Enhanced ITs in Winter

In order to further study the seasonal characteristics of ITs near the LS, the band-pass filtered, diurnal, and semidiurnal barotropic and baroclinic tidal currents throughout the whole observation period are shown in Figures 6 and 7, respectively. The diurnal baroclinic tidal currents are the strongest in winter; the largest diurnal baroclinic tidal currents are about 0.55 m/s and occur within depths of 53–69 m in the subsurface layer. The semidiurnal baroclinic tidal currents also have the largest magnitude (roughly 0.37 cm/s) within the same depths in winter. It reveals that the ITs are the strongest in winter at our observation site. The seasonally averaged, depth-integrated KE of barotropic and baroclinic diurnal and semidiurnal tidal currents are shown in

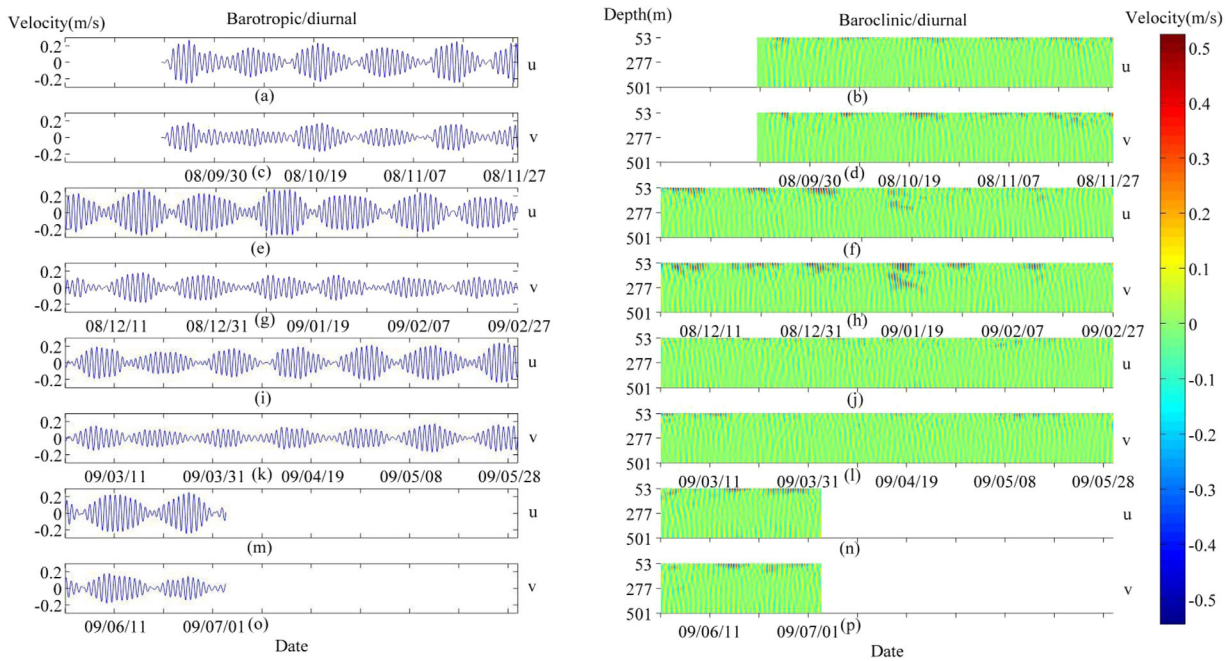


**Figure 6.** Time series of (a, e, i, m)  $u$  and (c, g, k, o)  $v$  components of the diurnal barotropic tidal currents versus depth in (i, k) spring, (m, o) summer, (a, c) autumn, and (e, g) winter. Time series of (b, f, j, n)  $u$  and (d, h, l, p)  $v$  components of the diurnal baroclinic tidal currents versus depth in (j, l) spring, (n, p) summer, (b, d) autumn, and (f, h) winter. The time axis is in the format of year/month/day.

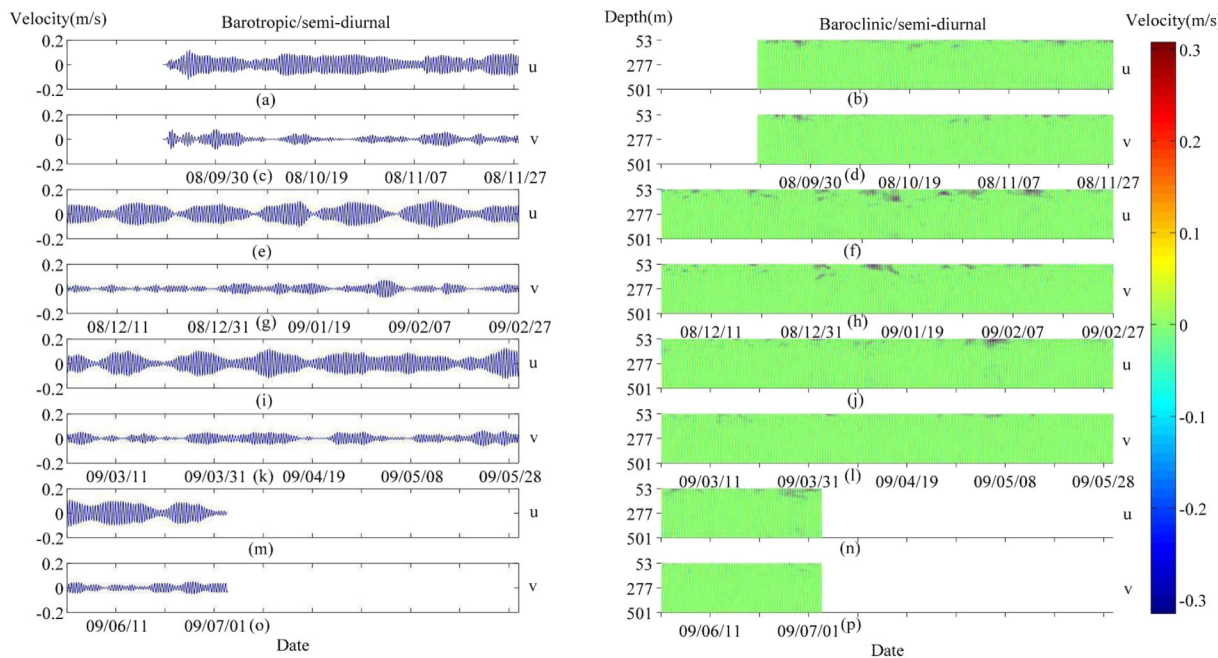


**Figure 7.** Same as Figure 6 except for the semidiurnal tidal currents.

Figure 8. It is found that in winter, the diurnal and semidiurnal barotropic tidal currents get the maximum and minimum ( $4.63$  and  $0.60 \text{ KJ/m}^2$ , respectively, while the corresponding baroclinic components both get the maximum ( $2.81$  and  $0.83 \text{ KJ/m}^2$ , respectively). Moreover, the seasonally averaged, depth-integrated KEDs of

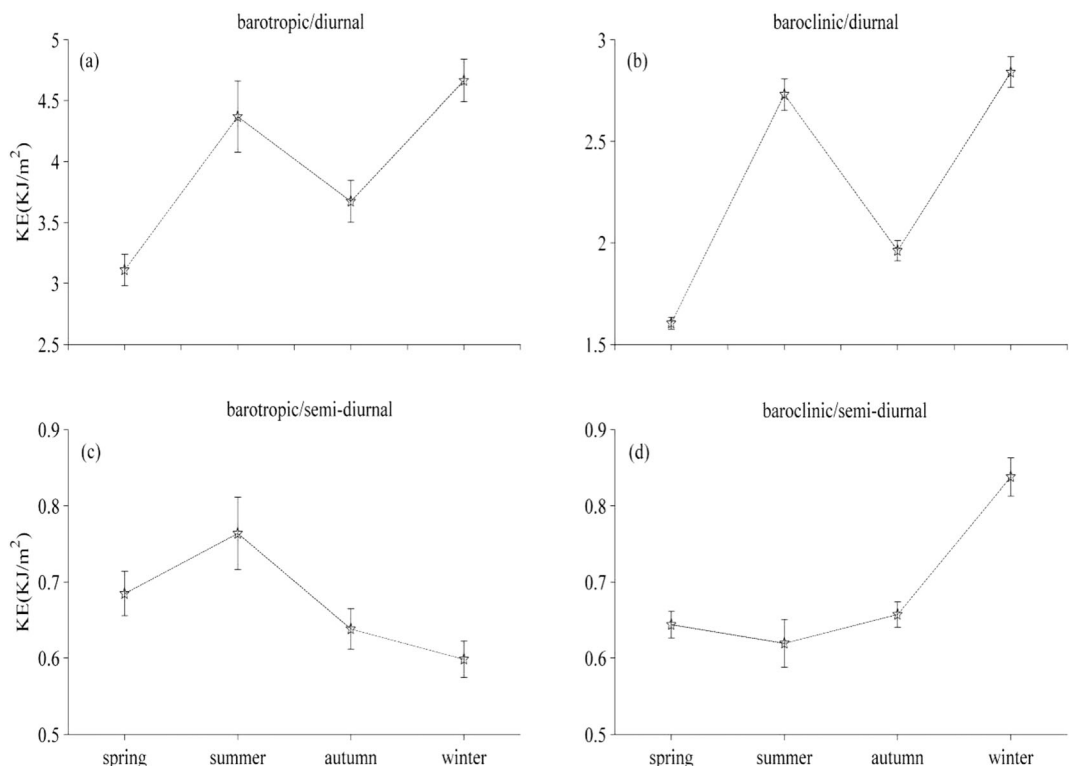


**Figure 8.** Seasonally averaged, depth-integrated KE of barotropic (a) diurnal and (c) semidiurnal baroclinic tidal currents. Seasonally averaged, depth-integrated KE of baroclinic (b) diurnal and (d) semidiurnal baroclinic tidal currents. Error bars (vertical lines) indicate the 95% statistical significance level hereafter.

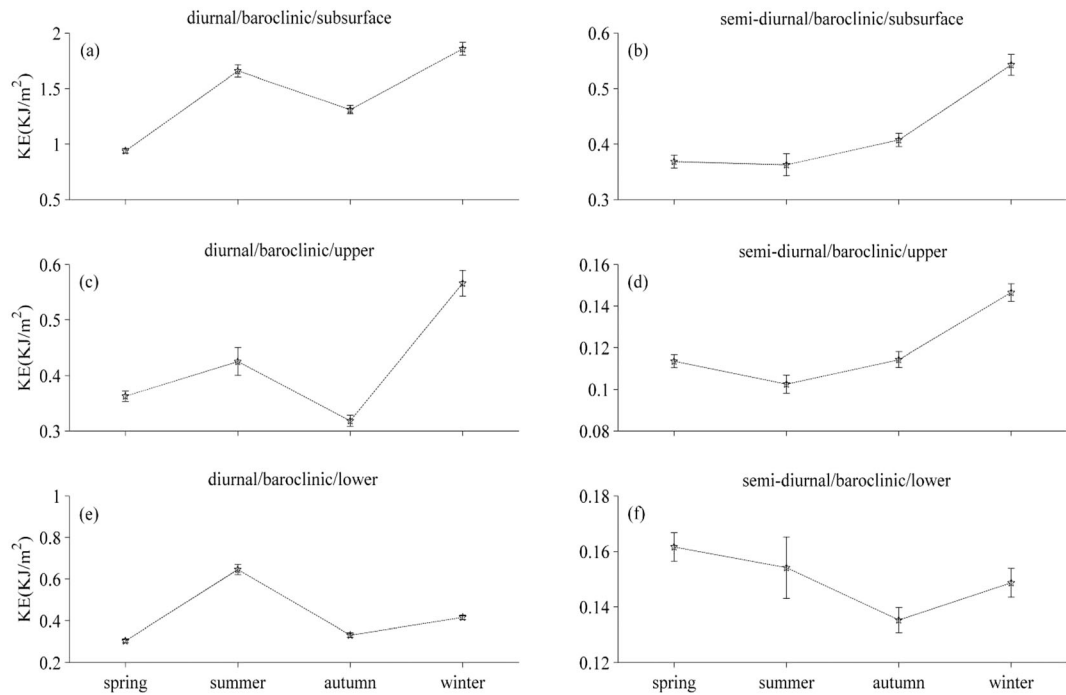


**Figure 9.** Seasonally averaged, depth-integrated KE of diurnal baroclinic tidal currents in (a) subsurface, (c) upper, and (e) lower layers, respectively. Seasonally averaged, depth-integrated KE of semidiurnal baroclinic tidal currents in (b) subsurface, (d) upper, and (f) lower layers, respectively.

diurnal and semidiurnal baroclinic tidal currents in the subsurface, upper and lower layers are shown in Figure 9. It is found that the diurnal and semidiurnal baroclinic tidal currents in the subsurface layer are the strongest throughout the year, e.g., the KED of diurnal (semidiurnal) baroclinic tidal currents in subsurface layer accounts for 64.8% (65.2%) of the KED throughout the whole water depth in winter when the diurnal (semidiurnal) baroclinic tidal currents are the strongest. The seasonal variation of diurnal baroclinic tidal currents is also much stronger than that of semidiurnal ones. Seasonal average, incoherent variances of the diurnal and semidiurnal ITs are shown in Figure 10. Our data show that baroclinic incoherent diurnal and semidiurnal variances account for the largest scale of diurnal and semidiurnal ITs in winter (Table 2), e.g., the  $u$  component of baroclinic incoherent diurnal (semidiurnal) variance accounts for about 86.6% (84.0%) of diurnal (semidiurnal) ITs in winter. Notably, it is found that the monthly averaged, depth-integrated semidiurnal baroclinic tidal currents in the subsurface, upper and lower layers all had the maximum in January 2009 in winter, with KEDs of 0.73, 0.20, and 0.21 KJ/m<sup>2</sup>, respectively (figure not shown). Moreover, the scales of the monthly average,  $u$  ( $v$ ) component of baroclinic incoherent semidiurnal motions over the semidiurnal ITs in the subsurface, upper and lower layers also all had the maximum in January 2009 in winter, with scales of 94.0% (95.7%), 94.1% (96.8%), and 94.5% (97.7%), respectively (figure not shown).

To further address the seasonal variability and vertical structure of diurnal and semidiurnal ITs, the EOF analysis method is used, e.g., Figures 11 and 12 and Table 3 show the modal structures in winter and PSDs of temporal variances for the first two modes of ITs in four seasons, respectively. Considering the  $u$  component is more closely correlated with the propagation of the ITs from LS, we will concentrate on the analysis of the  $u$  variations. It is observed that the uppermost reversal layer depths of the first (second)-mode wave are the deepest in spring and the shallowest in autumn for the  $u$  component, with the zero crossing points at 204.8 (107.1) m and 146.5 (73.4) m, respectively, and similar for the  $v$  component. The PSDs can represent the KEs of various modal ITs. It is found that the first-mode diurnal and semidiurnal ITs are both the strongest in winter, with PSDs of 139.4 and 37.2 (m/s)<sup>2</sup>/cph, respectively; the second-mode diurnal and semidiurnal ITs are also both the strongest in winter, with PSDs of 41.2 and 3.7 (m/s)<sup>2</sup>/cph, respectively. The first (second)-mode IT accounts for 54.9% (15.4%) of the energy variance for the  $u$  component, respectively, 42.5% (14.5%) for the  $v$  component, respectively. The modal structure of ITs makes no difference between diurnal and semidiurnal

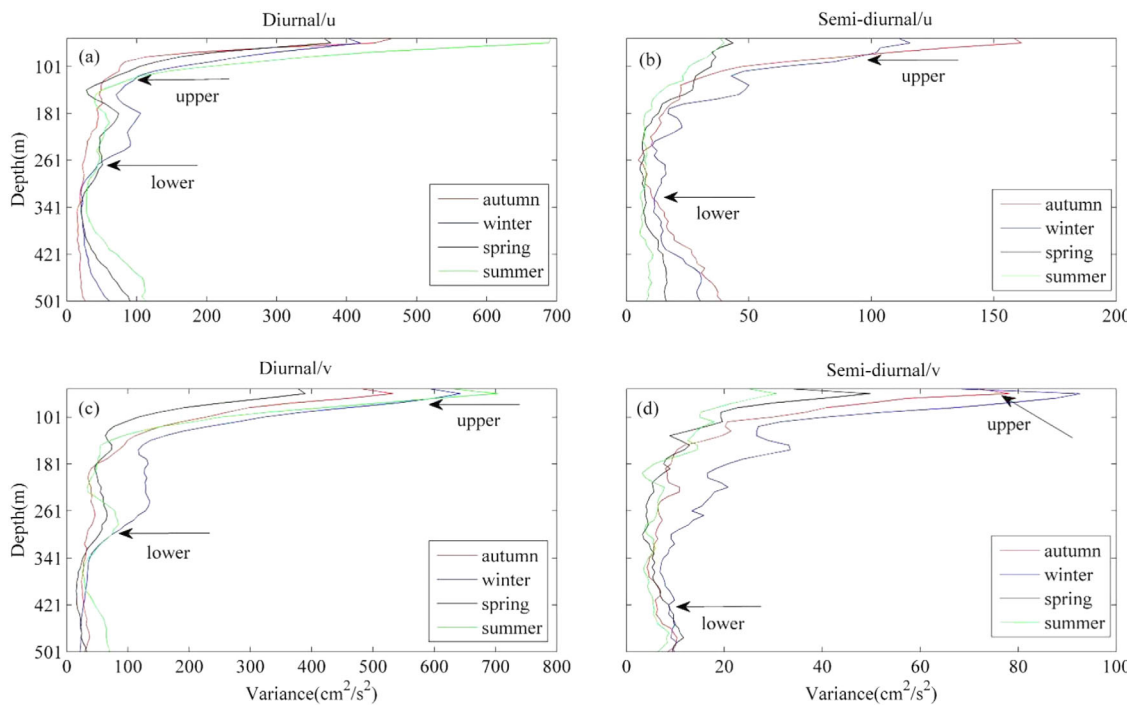


**Figure 10.** Seasonal average, incoherent current variances of (a, b)  $u$  and (c, d)  $v$  components of (a, c) diurnal and (b, d) semidiurnal ITs, respectively. Arrows denote the upper and lower layer depth where the incoherent variances were significant in winter.

constituents, as they are both dominated by the first-mode wave throughout the year, which is consistent with the results presented in Figure 4. Our conclusions are similar to those reported by Lee *et al.* [2012], but are somewhat different from those reported by Xu *et al.* [2013]. This is because the observation sites in this study and in Lee *et al.* [2012] are both quite close to the LS which is the generation source area of ITs. Therefore, the ITs at our observation site still retain a first-mode vertical structure after they propagate a short distance from the LS. However, after the long-range propagation to the continental slope, e.g., Dongsha Plateau, higher-mode ITs increase with distance from the source area [Xu *et al.*, 2013].

### 3.3. Discussion of the Mechanisms for Enhanced ITs in Winter

In order to investigate why the ITs are the strongest in winter at our observation site, the AVISO elevation data ([www.aviso.altimetry.fr](http://www.aviso.altimetry.fr)) within ( $19^{\circ}28' - 19^{\circ}28'N$ ,  $119^{\circ}57' - 119^{\circ}57'E$ ) during our observation period are used to detect if the eddies near our observation site are active or not (figure not shown). It is found that no strong eddies appear there in winter, i.e., the enhanced ITs in winter are not related to the eddy. It is suggested that the Kuroshio with high temperature and salinity makes important contribution to the vertical structure of the buoyancy frequency in the SCS [e.g., Xue *et al.*, 2004; Nan *et al.*, 2011], and Kuroshio intrusion is generally considered to be the strongest in winter [Shaw, 1991; Shaw and Chao, 1994]. Thus, we suggest that the significantly enhanced ITs in winter at our observation site may be induced by the Kuroshio intrusion into the SCS; the Kuroshio intrusion may form energetic mesoscale structures, lead to refraction of internal waves [Park and Farmer, 2013], and significantly enhance the diurnal and semidiurnal ITs in LS [Jan *et al.*, 2012]. However, the present study based on only mooring current observations without in situ temperature and salinity data is difficult to draw a solid conclusion. Furthermore, considering the complicated

**Table 2.** Seasonal Average Scales (%) of Baroclinic Incoherent Diurnal (Semidiurnal) Motions Over the Diurnal (Semidiurnal) ITs for  $u$  and  $v$  Current Components

	Diurnal				Semidiurnal			
	Spring	Summer	Autumn	Winter	Spring	Summer	Autumn	Winter
$u$	84.8	86.5	81.5	86.7	72.8	67.9	83.5	84.0
$v$	80.6	86.9	84.4	88.7	90.3	88.8	92.5	95.0

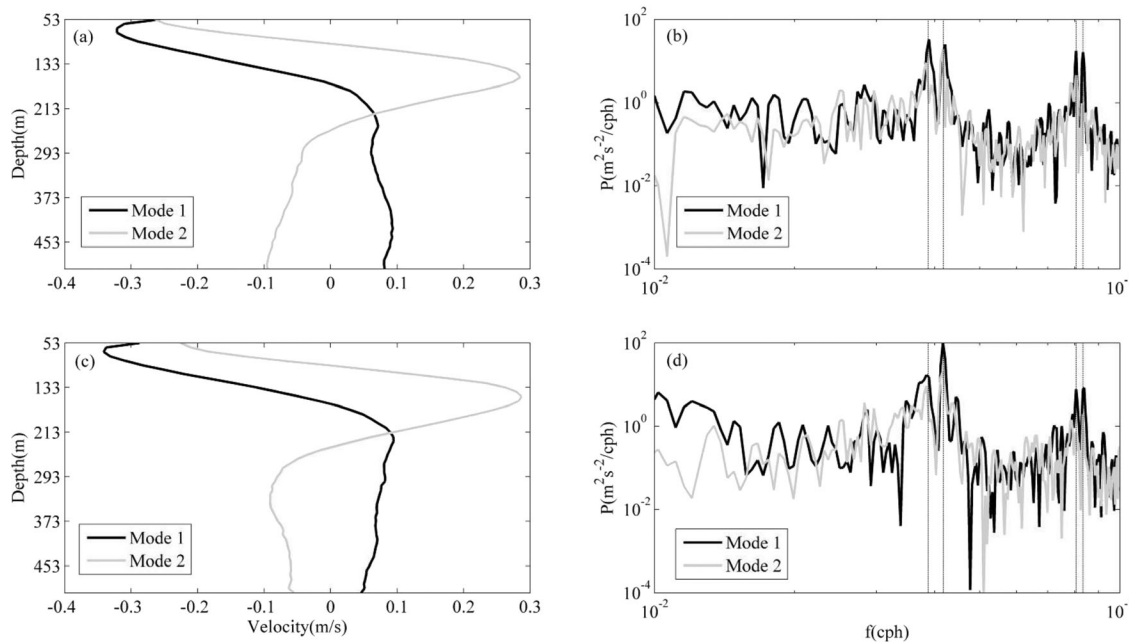


**Figure 11.** EOF analysis results of the (a, b)  $u$  and (c, d)  $v$  components of baroclinic currents in winter. (a, c) Vertical distribution of the first two baroclinic mode wave, (b, d) spectral density of eigenfunction time series for the first two baroclinic mode wave (where the four vertical lines from the left to the right denote where the frequencies of  $O_1$ ,  $K_1$ ,  $M_2$ , and  $S_2$  tidal constituents are situated, respectively).

topography and hydrography of the LS, the significantly enhanced ITs in winter could not be explained by only a single mechanism.

It is found that the  $v$  component of the first-mode diurnal ITs (with a PSD of  $115.9 (m/s)^2/cph$ ) are more significant than the  $u$  component (with a PSD of  $58.0 (m/s)^2/cph$ ) in winter. It seems to indicate that the enhanced ITs in winter are not related with the westward propagation of diurnal ITs from the LS. Thus, it is considered that the enhanced diurnal ITs in winter may be not only due to the Kuroshio intrusion but also

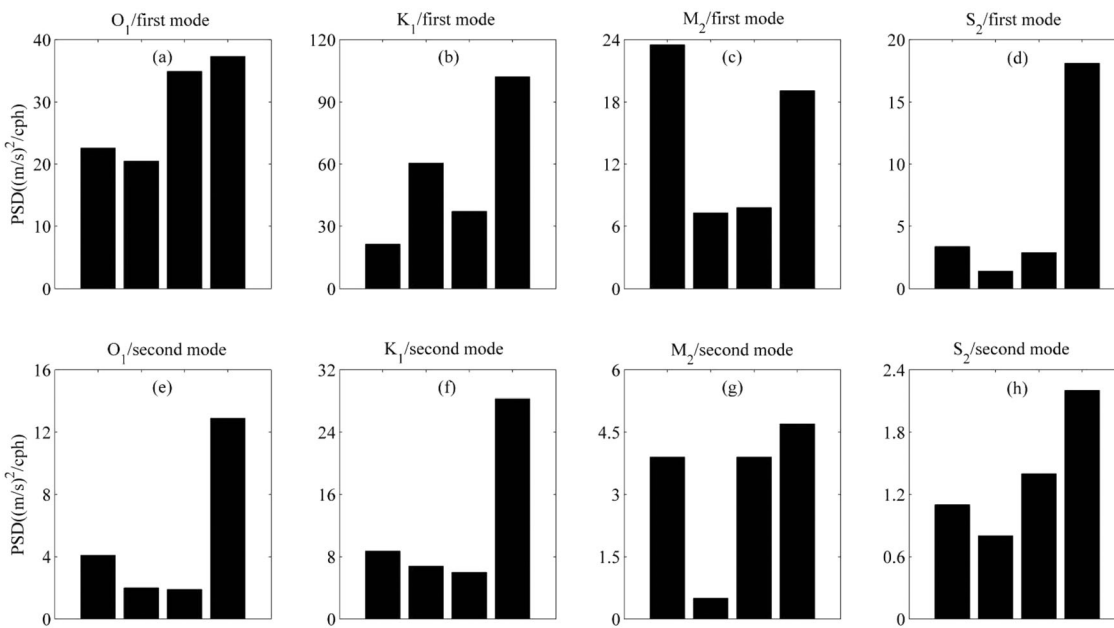


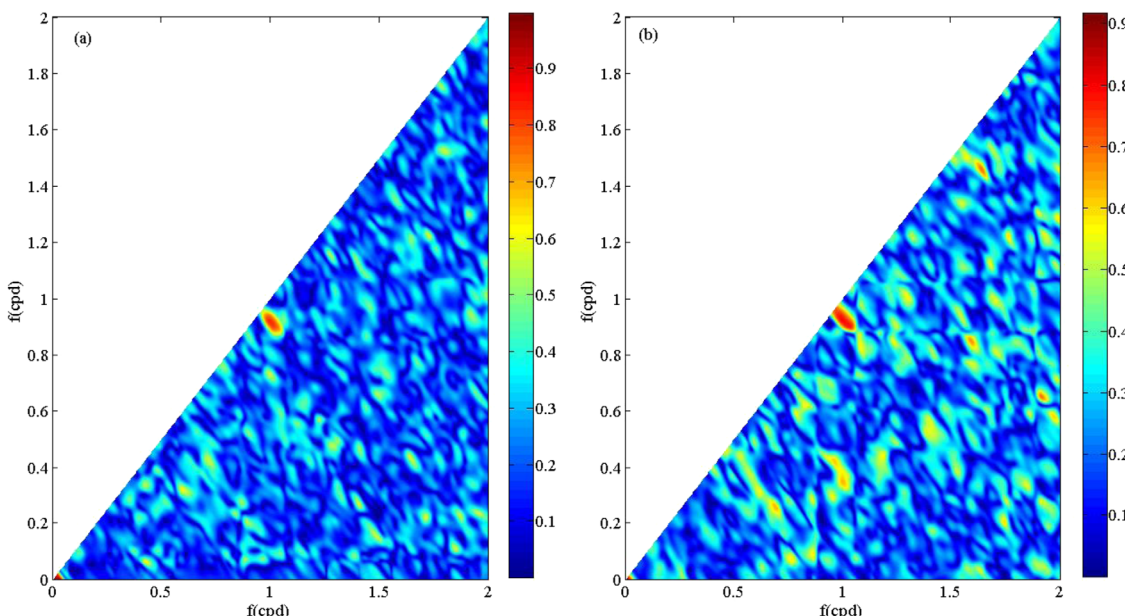
**Figure 12.** Seasonal PSDs ( $(m/s)^2/cph$ ) of the four major tidal constituents for the first two baroclinic mode waves. The bars in each subplot represent the PSDs of spring, summer, autumn, and winter from the left to the right, respectively.

**Table 3.** Seasonal Uppermost Reversal Layer Depths (m) for the First Two Baroclinic Mode Waves

	Spring	Summer	Autumn	Winter
First-mode ITs	191.8	189.4	151.9	165.7
Second-mode ITs	100.0	102.2	79.6	95.2

the enhanced diurnal barotropic tidal currents during that period (Figure 8). However, it is not clear why the semidiurnal ITs were also enhanced in winter, even when the corresponding barotropic tidal currents are the weakest throughout the year (also, see Figure 8).

To investigate if there exists nonlinear interaction among different constituents ITs, the averaged bicoherence of  $u$  and  $v$  components of the baroclinic currents in the subsurface, upper and lower layers in four seasons are calculated (e.g., Figure 13 shows the results in subsurface layer in winter). It is found that only in the subsurface layer in winter there is a significant bicoherence value at (0.93 and 1.00 cpd). It seems to indicate a nonresonant (strong) nonlinear interaction between diurnal IT constituents  $O_1$  and  $K_1$  in the subsurface layer in winter, i.e., a harmonic semidiurnal wave (hereafter referred to as  $D_2$ ), with a frequency of 1.93 cpd (i.e., 0.93 + 1.00 cpd is the sum of the frequencies of constituents  $O_1$  and  $K_1$ , noting that it is equal to the frequency of constituent  $M_2$ ) is generated via nonlinear interaction between diurnal IT constituents  $O_1$  and  $K_1$ , and thus subsequently enhances the semidiurnal internal tidal currents. It is found that there are at least two obvious difference between Wang [2012] and our study: (1) Wang [2012] suggests that the diurnal modulation is caused by interaction of barotropic diurnal tidal currents with the linear internal waves; but we suggest that the diurnal modulation is caused by the interaction of baroclinic  $K_1$  and  $O_1$  diurnal ITs; (2) Wang [2012] assumes there is no interaction between the semidiurnal and diurnal tidal bands in calculating energy balance, which is generally not valid as the energy spectrum is continuous; but we suggest that there exists an interaction between the semidiurnal and diurnal tidal bands, which results in the enhanced ITs in winter. Furthermore, the seasonal vertical shear spectra of baroclinic currents at each bin depth throughout the whole water depth are calculated (e.g., Figure 14 shows the results in the subsurface layer in four seasons). It is found that the PSDs in diurnal and semidiurnal frequency bands both have their maximum in the subsurface layer in winter. The PSDs in semidiurnal frequency band also show remarkable peaks only in the subsurface layer in winter, especially at the frequency of constituent  $M_2$ ; otherwise, the semidiurnal band shows white spectra without any spectral peak. The seasonal, depth-averaged shears of diurnal baroclinic tidal currents in the subsurface, upper and lower layers are shown in Figure 15. It is evident that the seasonal shears of diurnal baroclinic tidal currents in the subsurface and upper layers both have their

**Figure 13.** Averaged bicoherence spectra of (a)  $u$  and (b)  $v$  components of the total observed currents in winter in subsurface layer, respectively.

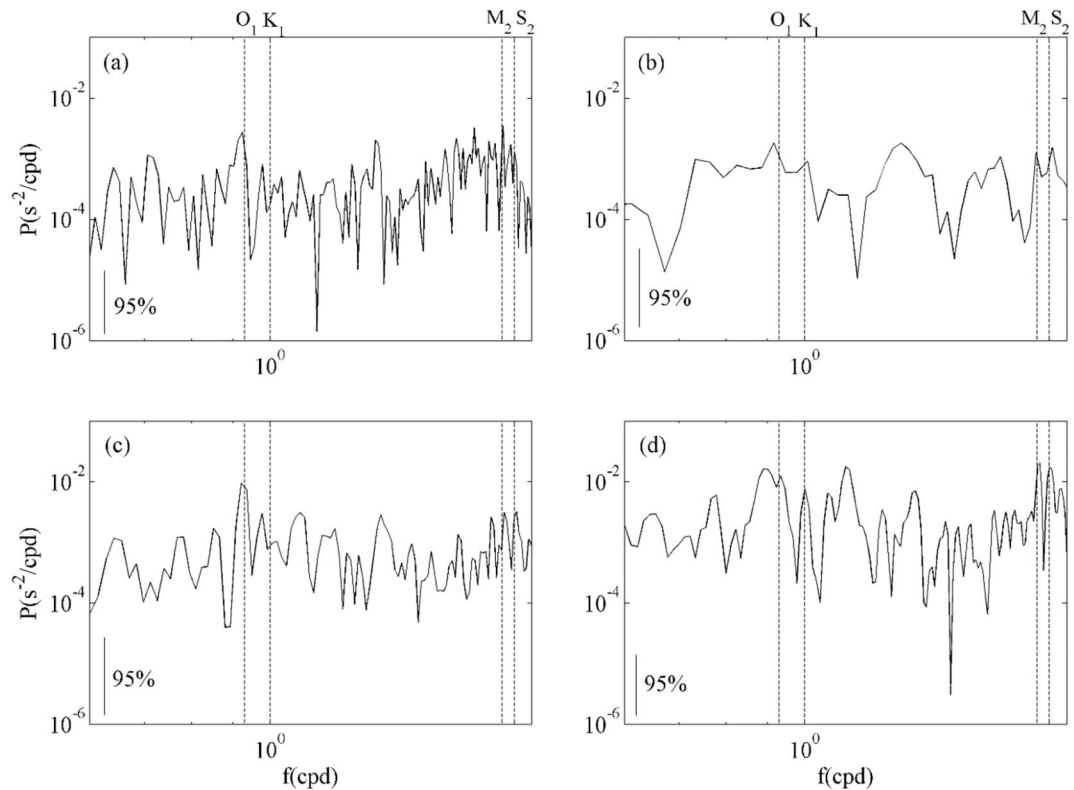


**Figure 14.** Shear spectra (black lines) of the baroclinic currents in subsurface layer in (a) spring, (b) summer, (c) autumn, and (d) winter, respectively. The short vertical bars near the left lower corners indicate the 95% statistical significance level.

maximum in winter. These seem to suggest that the strong nonlinear interaction between IT constituents  $O_1$  and  $K_1$  may be attributed to the high vertical shear of diurnal ITs in the subsurface layer in winter, which favors the conclusion that the vertical shear aroused by original frequency can induce motions of nonlinear interactions frequencies [Xing and Davies, 2002].

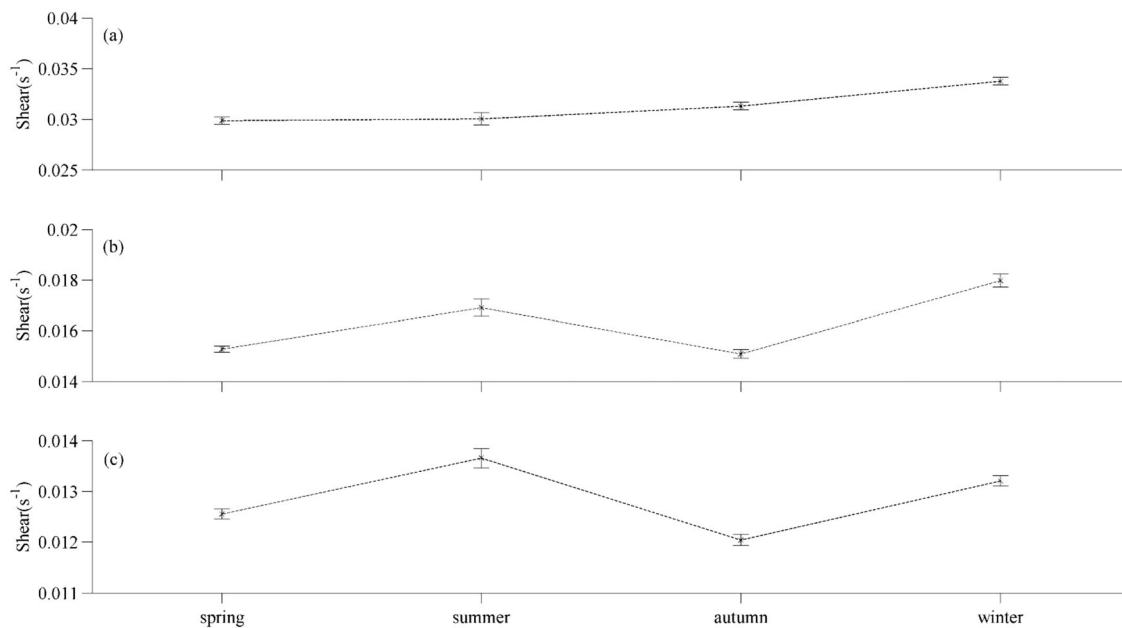


**Figure 15.** Seasonal depth-averaged shears of the diurnal baroclinic tidal currents in (a) subsurface, (b) upper, and (c) lower layers, respectively.

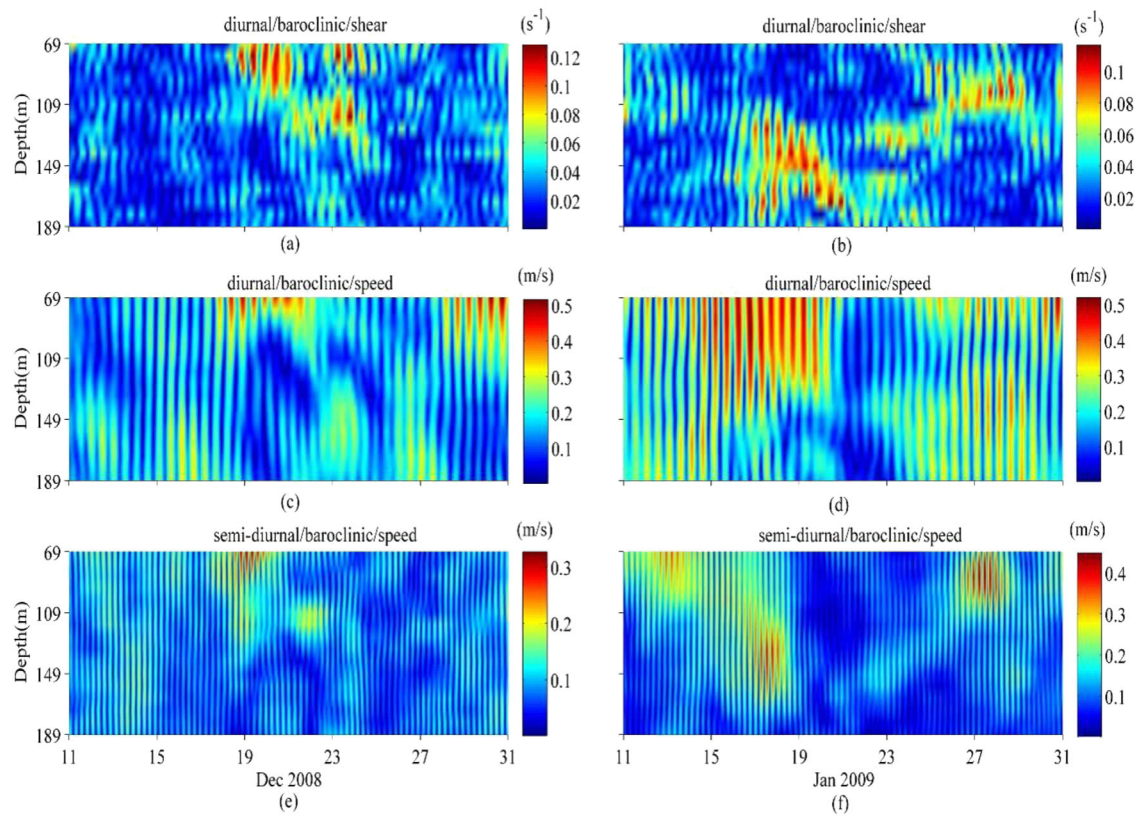


**Figure 16.** Time series of the 8 m shear magnitude of the diurnal baroclinic currents versus depth in subsurface layer in (a) December 2008 and (b) January 2009. Time series of the diurnal baroclinic current magnitude versus depth in subsurface layer in (c) December 2008 and (d) January 2009. Time series of the semidiurnal baroclinic current magnitude versus depth in subsurface layer in (e) December 2008 and (f) January 2009. The x axis is in the format of day.

To further ascertain this conclusion, simultaneous magnitudes of diurnal baroclinic current shears and semidiurnal baroclinic tidal currents in the subsurface layer are calculated. It is found that from 18 to 20 December 2008, the strongest semidiurnal baroclinic tidal currents appear within depths of 69–100 m, where the diurnal baroclinic tidal current shear is also the largest (Figures 16a and 16e). Similarly, from 16 to 19 January 2009 within depths of 120–160 m, and from 25 to 27 January 2009 within depths of 69–110 m, there is also strong correlation between the largest diurnal baroclinic tidal current shear and semidiurnal baroclinic tidal currents (Figures 16b and 16f), i.e., when and where the diurnal baroclinic tidal current shears are large, semidiurnal baroclinic tidal currents are greatly intensified, large diurnal baroclinic tidal current shear, and large semidiurnal baroclinic tidal current concur in temporal and spatial domains. Furthermore, it is found that the variations of the shear of  $u$  and  $v$  components (figures omitted, especially for the shear of  $u$  component) are approximately the same as that of the shear magnitude of current velocity. This seems to confirm that the nonlinear interaction between diurnal IT constituents  $K_1$  and  $O_1$  is due to the high vertical shear of diurnal ITs in the subsurface layer; thus, a harmonic semidiurnal constituent  $D_2$  is induced and subsequently enhances the energy of constituent  $M_2$ . However, it is important to note that the diurnal ITs are the energy source for the strong nonlinear interaction; thus, although there is a strong diurnal shear signal near the surface on 23 December, the diurnal ITs are relatively weak near the surface at that time (Figure 16c) and, therefore, there are no enhanced semidiurnal ITs. Second, there is no strong diurnal signal near the subsurface on 12 January, but there does exist enhanced semidiurnal ITs. This indicates that the nonlinear interaction may not be the only way for the enhanced semidiurnal motions to be generated in winter. Finally, the diurnal ITs are also enhanced in similar duration in Figure 16. Thus, we suggest that these possible mechanisms for the enhanced ITs in winter of LS may exert effects synchronously.

While the nonlinear interaction occurs in the subsurface layer, it is not clear why the semidiurnal ITs are also enhanced in winter in the upper and lower layers. The wave number rotary spectra of semidiurnal baroclinic tidal

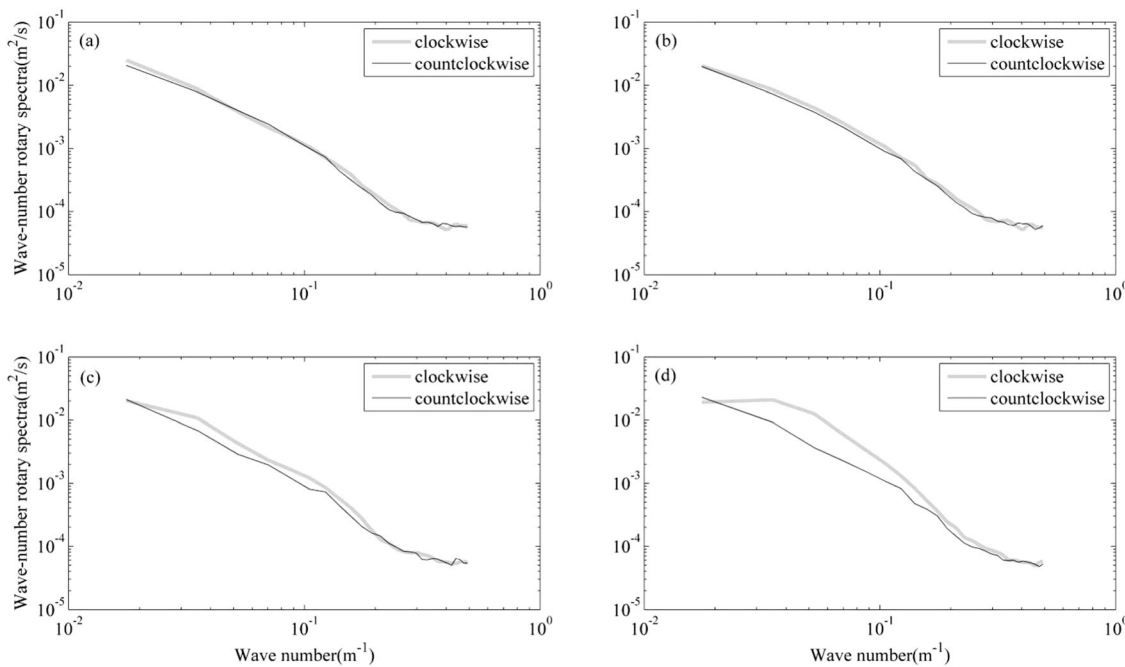


**Figure 17.** Wave number rotary spectra of the semidiurnal baroclinic currents in (a) spring, (b) summer, (c) autumn, and (d) winter, respectively.

currents during the four seasons are shown in Figure 17. It is found that only in winter,  $C_m \cdot A_m$  is positive and rather large, indicating that the energy source locates in the subsurface layer where the energy propagates downward intensively. This further suggests that the dramatic semidiurnal IT constituent  $D_2$  in the subsurface layer induced by nonlinear interaction might be a major mechanism for the energy propagating from the subsurface layer to upper and lower layers. In other words, the enhanced semidiurnal ITs in upper and lower layers in winter might be brought about indirectly by IT constituent  $D_2$  induced in the subsurface layer by nonlinear interaction.

#### 4. Conclusions

In this paper, based on harmonic analysis, spectral analysis and EOF methods, the seasonal characteristics and nonlinear interaction of ITs near the LS in the northeastern SCS are studied by 285 day, in situ current data. The following conclusions can be drawn.

First, the highest KEDs of diurnal and semidiurnal baroclinic tidal currents are 2.81 and 0.83 KJ/m<sup>2</sup> in winter, respectively. ITs in the subsurface layer are the strongest throughout the year, and the incoherent ITs fluctuations are overwhelmingly dominant during the entire observation period, especially in winter.

Second, the diurnal and semidiurnal ITs are both dominated by the first-mode wave throughout the year. The first and second-mode diurnal (semidiurnal) ITs are both the strongest in winter. The uppermost reversal layer depths of the first (second)-mode wave are the deepest in spring and the shallowest in autumn, with the zero crossing points at 204.8 (107.1) m and 146.5 (73.4) m, respectively.

Third, the enhanced diurnal ITs in winter may be due to the enhanced diurnal barotropic tidal currents, while the enhanced semidiurnal ITs in winter may be caused by the strong nonlinear interaction between diurnal IT constituents  $O_1$  and  $K_1$  due to their high vertical shears in the subsurface layer. Thus, the harmonic semidiurnal constituent  $D_2$  with a similar frequency of constituent  $M_2$  is induced; it subsequently enhances the first-mode semidiurnal ITs in this layer, and the associated energy is carried downward to enhance the semidiurnal ITs in upper and lower layers. However, the nonlinear interaction may not be the only way for the enhanced semidiurnal motions generated in winter.

Lastly, the significantly enhanced ITs in winter at our observation site may be also induced by the Kuroshio intrusion into the SCS in winter. Moreover, the location of our mooring site is near the southern end of the LS and is not on the main pathway of the propagation of internal tides, as suggested by various studies.

Thus, the observed enhanced ITs in winter similarly show that the ITs generation in LS may be a complicated three-dimensional problem, which is somewhat inconsistent with previous modal works [e.g., Niwa and Hibiya, 2004; Jan et al., 2007; 2008].

### Acknowledgments

The data for this paper can be requested from Shuqun Cai by e-mail: caisq@scsio.ac.cn. This work was jointly supported by the Strategic Priority Research Program of the Chinese Academy of Sciences (XDA11020201), National Basic Research Program (2013CB956101), NSFC grant (41406023, 41206009, 41430964, 41521005, and 41025019), the CAS/SAFEA International Partnership Program for Creative Research Teams (20140491532), and the Innovation Group Program (LTOZZ1502) of State Key Laboratory of Tropical Oceanography (South China Sea Institute of Oceanology, Chinese Academy of Sciences). We also thank Stacey Ollis for her editing service and the anonymous reviewers for critical comments.

### References

- Alford, M. H. (2008), Observations of parametric subharmonic instability of the diurnal internal tide in the South China Sea, *Geophys. Res. Lett.*, 35, L15602, doi:10.1029/2008GL034720.
- Cai, S. Q., Z. J. Gan, and X. M. Long (2002), Some characteristics and evolution of the internal soliton in the northern South China Sea, *Chin. Sci. Bull.*, 47, 21–26.
- Cai, S. Q., J. X. Xu, J. L. Liu, Z. W. Chen, J. S. Xie, J. Li, and Y. H. He (2015), Retrieval of the maximum horizontal current speed induced by ocean internal solitary waves from low resolution time series mooring data based on the KdV theory, *Ocean Eng.*, 94, 88–93.
- Carter, G. S., and M. C. Gregg (2006), Persistent near-diurnal internal waves observed above a site of  $M_2$  barotropic-to-baroclinic conversion, *J. Phys. Oceanogr.*, 36, 1136–1147.
- Egbert, G. D., and S. Y. Erofeeva (2002), Efficient inverse modeling of barotropic ocean tides, *J. Atmos. Oceanic Technol.*, 19, 183–204.
- Elgar, S., and R. T. Guza (1988), Statistics of bicoherence, *IEEE Trans. Acoust. Speech Signal Process.*, 36, 1667–1668.
- Garrett, C. J. R., and W. H. Munk (1972), Space-time scales of internal waves, *Geophys. Fluid Dyn.*, 2, 225–264.
- Garrett, C. J. R., and W. H. Munk (1975), Space-time scales of internal waves: A progress report, *J. Geophys. Res.*, 80, 291–297.
- Hinich, M. J., and M. Wolinsky (2005), Normalizing bispectra, *J. Stat. Plann. Inference*, 130, 405–411.
- Jan, S., C.-S. Chern, J. Wang, and M.-D. Chiou (2012), Generation and propagation of baroclinic tides modified by the Kuroshio in the Luzon Strait, *J. Geophys. Res.*, 117, C02019, doi:10.1029/2011JC007229.
- Jan, S., C.-S. Chern, J. Wang, and S.-Y. Chao (2007), Generation of diurnal K1 internal tide in the Luzon Strait and its influence on surface tide in the South China Sea, *J. Geophys. Res.*, 112, C06019, doi:10.1029/2006JC004003.
- Jan, S., R. C. Lien, and C. H. Ting (2008), Numerical study of baroclinic tides in Luzon Strait, *J. Oceanogr.*, 64, 789–802.
- Kim, Y. C., and E. J. Powers (1979), Digital bispectral analysis and its application to nonlinear wave interactions, *IEEE Trans. Plasma Sci.*, 7, 120–131.
- Klymak, J. M., M. H. Alford, and P. Pinkel (2011), The breaking and scattering of the internal tide on a continental slope, *J. Phys. Oceanogr.*, 41, 926–945.
- Leaman, K. D., and T. B. Sanford (1975), Vertical energy propagation of internal waves: A vector spectral analysis of velocity profiles, *J. Geophys. Res.*, 80, 1975–1978.
- Lee, I. H., Y. H. Wang, Y. Yang, and D. P. Wang (2012), Temporal variability of internal tides in the northeast South China Sea, *J. Geophys. Res.*, 117, C02013, doi:10.1029/2011JC007518.
- Liao, G. H., Y. C. Yuan, K. Arata, C. H. Chen, T. Naokazu, G. Noriaki, and M. Masanori (2011), Analysis of internal tidal characteristics in the layer above 450 m from acoustic Doppler current profiler observations in the Luzon strait, *Sci. China Earth Sci.*, 54, 1078–1094.
- Lien, R. C., T. Y. Tang, M. H. Chang, and E. A. D'Asaro (2005), Energy of nonlinear internal waves in the South China Sea, *Geophys. Res. Lett.*, 32, L05615, doi:10.1029/2004GL022012.
- Muller, P., G. Holloway, F. Henyey, and N. Pomphrey (1986), Nonlinear interactions among internal gravity waves, *Rev. Geophys.*, 24, 493–536.
- Nan, F., H. Xue, F. Chai, L. Shi, M. Shi, and P. Guo (2011), Identification of different types of Kuroshio intrusion into the South China Sea, *Ocean Dyn.*, 61, 1291–1304, doi:10.1007/s10236-011-0426-3.
- Niwa, Y., and T. Hibiya (2004), Three-dimensional numerical simulation of  $M_2$  internal tides in the East China Sea, *J. Geophys. Res.*, 109, C04027, doi:10.1029/2003JC001923.
- Park, J. H., M. Andres, P. J. Martin, M. Wimbush, and D. R. Watts (2006), Second-mode internal tides in the East China Sea deduced from historical hydrocasts and a model, *Geophys. Res. Lett.*, 33, L05602, doi:10.1029/2005GL024732.
- Park, J. H., and D. Farmer (2013), Effects of Kuroshio intrusions on nonlinear internal waves in the South China Sea during winter, *J. Geophys. Res. Oceans*, 118, 7081–7094, doi:10.1002/2013JC008983.
- Pawlowski, R., R. Beardsley, and S. Lentz (2002), Classical tidal harmonic analysis including error estimates in MATLAB using T\_TIDE, *Comput. Geosci.*, 28, 929–937.
- Shaw, P. T. (1991), The seasonal variation of the intrusion of the Philippine Sea water into the South China Sea, *J. Geophys. Res.*, 96, 821–827, doi:10.1029/90JC02367.
- Shaw, P. T., and S. Y. Chao (1994), Surface circulation in the South China Sea, *Deep Sea Res., Part I*, 41, 1663–1683.
- St. Laurent, L., and C. Garrett (2002), The role of internal tides in mixing the deep ocean, *J. Phys. Oceanogr.*, 32, 2882–2899.
- Sun, L., Q. A. Zheng, D. X. Wang, J. Y. Hu, C. K. Tai, and Z. Y. Sun (2011), A case study of near-inertial oscillation in the South China Sea using mooring observations and satellite altimeter data, *J. Oceanogr.*, 67, 677–687, doi:10.1007/s10872-011-0081-9.
- van Haren, H. (2004), Some observations of nonlinearly modified internal wave spectra, *J. Geophys. Res.*, 109, C03045, doi:10.1029/2003JC002136.
- van Haren, H. (2005), Tidal and near-inertial peak variations around the diurnal critical latitude, *Geophys. Res. Lett.*, 32, L23611, doi:10.1029/2005GL024160.
- Vlasenko, V., N. Stashchuk, C. Guo, and X. Chen (2010), Multimodal structure of baroclinic tides in the South China Sea, *Nonlinear Proc. Geophys.*, 17, 529–543.
- Wang, D. P. (2012), Diurnal modulation of semidiurnal internal tides in Luzon Strait, *Ocean Model.*, 59–60, 1–10.
- Xie, X. H., G. Y. Chen, X. D. Shang, and D. X. Wang (2008), Evolution of the semidiurnal ( $M_2$ ) internal tide on the continental slope of the northern South China Sea, *Geophys. Res. Lett.*, 35, L13604, doi:10.1029/2008GL034179.
- Xie, X. H., X. D. Shang, and G. Y. Chen (2010), Nonlinear interactions among internal tidal waves in the northeastern South China Sea, *Chin. J. Oceanol. Limnol.*, 28, 996–1001.
- Xing, J., and A. M. Davies (2002), Processes influencing the nonlinear interaction between inertial oscillations, near inertial internal waves and internal tides, *Geophys. Res. Lett.*, 29(5), 1067, doi:10.1029/2001GL014199.
- Xu, Z. H., B. S. Yin, Y. J. Hou, and Y. S. Xu (2013), Variability of internal tides and near-inertial waves on the continental slope of the northwestern South China Sea, *J. Geophys. Res. Oceans*, 118, 197–211, doi:10.1029/2012JC008212.
- Xu, Z. H., B. S. Yin, Y. J. Hou, Y. S. Xu, and A. K. Liu (2014), Seasonal variability and north-south asymmetry of internal tides in the deep basin west of the Luzon Strait, *J. Mar. Syst.*, 134, 101–122.
- Xue, H., F. Chai, N. Pettigrew, D. Xu, M. Shi, and J. Xu (2004), Kuroshio intrusion and the circulation in the South China Sea, *J. Geophys. Res.*, 109, C02017, doi:10.1029/2002JC001724.